ADVANCED FUNCTIONAL MATERIALS
www.afm-journal.de

On the Role of the $Sr_{3-x}Ca_xAl_2O_6$ Sacrificial Layer Composition in Epitaxial $La_{0.7}Sr_{0.3}MnO_3$ Membranes

*Pol Salles, Roger Guzman, Aleix Barrera, Martí Ramis, Jose Manuel Caicedo, Anna Palau, Wu Zhou, and Mariona Coll**

The possibility to fabricate freestanding single crystal complex oxide films has raised enormous interest to be integrated in next-generation electronic devices envisaging distinct and novel properties that can deliver unprecedented performance improvement compared to traditional semiconductors. The use of the water-soluble $Sr_3Al_2O_6$ (SAO) sacrificial layer to detach the complex oxide film from the growth substrate has significantly expanded the complex oxide perovskite membranes library. Nonetheless, the extreme water sensitivity of SAO hinders its manipulation in ambient conditions and restricts the deposition approaches to those using high vacuum. This study presents a pioneering study on the role of Ca-substitution in solution processed SAO ($Sr_{3-x}Ca_xAl_2O_6$ with $x \leqslant 3$) identifying a noticeable improvement on surface film crystallinity preserving a smooth surface morphology while favoring the manipulation in a less-restricted ambient conditions. Then, the study focuses on the effect of the sacrificial composition on the subsequent ex situ deposition of $La_{0.7}Sr_{0.3}MnO_3$ (LSMO) by pulsed laser deposition, to obtain epitaxial films with a variable degree of strain. Finally, epitaxial and strain-free LSMO membranes with metal-insulator transition at 290 K are delivered. This study offers a hybrid and versatile approach to prepare and easily manipulate crystalline perovskite oxide membranes by facilitating ex situ growth on SAO-based sacrificial layer.

1. Introduction

Next generation electronic devices are facing a rapidly advancing technological development to respond to the evolving needs of today's society and its future expected challenges. Within these technological advances, novel and multifunctional device concepts are starting to attract interest.[1–3] Complex transition-metal oxides, in particular ABO_3 perovskite oxides, are a promising family of materials that offer a wide range of properties including ferroelectricity,[4] multiferroicity,[5] metal-insulator transitions,[6] magnetism, and superconductivity,[7] to name a few.[8] These properties are affected by the oxide structure, crystalline quality, and presence of defects requiring the growth of such materials to be precise, constrained on specific crystalline substrates and to be processed at high temperature[9–12] which significantly limit their unprecedented opportunities. Nonetheless, in the last few years this field has experienced a major turn boosted by the development of synthetic approaches to detach these epitaxial oxides from the growth substrate and freely manipulate them.[13–15] In fact, the fabrication of new artificial heterostructures by assembling very dissimilar materials, their integration in conventional materials such as silicon, plastics, and 2D semiconductors,[16–18] and the possibility to obtain spontaneous shaped structures [19] is becoming a reality opening the possibility to study novel interface phenomena, nanoengineer their properties, and unlock strain states that might not be available by traditional epitaxial growth.[20–22]

The use of a sacrificial layer is an appealing approach to fabricate and manipulate freestanding epitaxial complex oxides membranes.[23] This method consists of adding a buffer layer between the substrate and the complex oxide that ensures epitaxial growth and the subsequent detachment upon selective etching. Recently, $Sr_3Al_2O_6$ (SAO) has been proved successful to be used as water-soluble sacrificial layer.[24–26] SAO has a pseudoperovskite structure (Pa-3) with a cubic unit cell (a = 15.844 Å; a/4 = 3.961 Å)[27] which is close to four times the lattice constant of $SrTiO_3$ (STO, a = 3.905 Å), a typical monocrystalline substrate used for the growth of different perovskite oxides.[28] The SAO structure consists of

P. Salles, A. Barrera, M. Ramis, A. Palau, M. Coll
ICMAB-CSIC
Campus UAB, Bellaterra, Barcelona 08193, Spain
E-mail: mcoll@icmab.es
R. Guzman, W. Zhou
School of Physical Sciences
University of Chinese Academy of Sciences
Beijing 100049, China
J. M. Caicedo
Catalan Institute of Nanoscience and Nanotechnology (ICN2)
Campus UAB, Bellaterra 08193, Barcelona, Spain

The ORCID identification number(s) for the author(s) of this article can be found under https://doi.org/10.1002/adfm.202304059

DOI: 10.1002/adfm.202304059

discrete Al-O networks based on rings of six AlO_4 tetrahedra ($Al_6O_{18}^{18-}$) with two nonbridging oxygen bonds with Sr^{2+} ions. Because Al^{3+} is more electronegative than Sr^{2+}, Sr-O bonding has a more ionic character than Al-O. When exposed to water, the easy protonation of this Sr-O ionic bonding is the responsible of the fast hydrolysis of the structure, which makes SAO a suitable sacrificial layer to be etched with water.[29,30] However, despite these wealthy properties, SAO still presents some challenges that need to be overcome to exploit its full potential.

First, while its high reactivity with water makes it almost the perfect candidate for selective etching against many perovskite oxides,[23] it also helps the fast development of an amorphous capping layer when exposed to air.[31] This reactivity hinders the subsequent epitaxial growth of the perovskite oxide. The use of a protective $SrTiO_3$ layer [32] can partially help fixing the sacrificial instability issue, although it brings some limitations to prepare stacked membrane heterostructures with pristine interfaces. [33] Also, the softness of the SAO structure can give rise to cation interdiffusion at the interface during the high temperature growth of the complex oxide, as it was reported for the $La_{0.7}Sr_{0.3}MnO_3$/SAO system,[34] which can hinder the membrane exfoliation and alters its functional properties. Finally, the growth of complex oxides on mismatched SAO can produce cracked and wrinkled membranes upon exfoliation as a mechanism for strain release. [20] It is worth noting that the detachment of a faultless membrane, regardless of the nature of the sacrificial layer, remains a key challenge in the preparation of freestanding films.[35,36]

A simple way to modify the properties of SAO is to engineer the metal-oxygen bond through cation substitution. The higher the M^{2+} electronegativity ($Ca^{2+} > Sr^{2+} > Ba^{2+}$), the lower its bonding ionicity with the nonbridging oxygens of the structure, and thus it is more difficult to hydrolyze. Consequently, $Ca_3Al_2O_6$ is dissolved much slower in water than $Ba_3Al_2O_6$.[37] Additionally, the difference in cation size ($Ba^{2+} > Sr^{2+} > Ca^{2+}$) enables tuning the SAO lattice parameter ranging from a/4 = 4.125 Å for $Ba_3Al_2O_6$ to a/4 = 3.816 Å for $Ca_3Al_2O_6$[30] providing a platform of sacrificial layers that can accommodate many different perovskite oxides with different strain states being a powerful tool to modulate the physical properties of the epitaxial oxide membrane.[20,37–39]

$La_{0.7}Sr_{0.3}MnO_3$ (LSMO) is an attractive perovskite oxide with extraordinary electrical and magnetic properties making the material an appealing candidate for spintronics and memory devices.[6,40–42] The growth of high quality LSMO membranes is also of crucial importance where slight variation in strain,[43–45] crystal orientation,[46] oxygen stoichiometry[47,48] and Sr doping[49] can significantly affect its properties. The preparation of flexible and epitaxial LSMO has already been attempted by high-vacuum deposition processes using mica substrates[50,51] and sacrificial layers such as $YBa_2Cu_3O_7$[52] and SAO.[24,34,53,54] Here we go one step further in developing a hybrid and versatile synthetic approach for LSMO membranes, based on solution-processed $Sr_{3-x}Ca_xAl_2O_6$ with $x \leqslant 3$ (SC_xAO) sacrificial layers in which ambient stability and crystallinity are improved upon Ca-substitution while preserving smooth surface morphology, demonstrated by means of reflection high energy electron diffraction (RHEED), scanning transmission electron microscopy (STEM), x-ray diffraction (XRD) and atomic force microscopy (AFM). Then it is discussed how SC_xAO composition affects the ex situ deposition of pulsed laser deposited (PLD) LSMO films on their crystallinity, strain, interface cation diffusion, and electrical properties. Finally, the properties of the exfoliated LSMO membranes are presented, demonstrating the feasibility to integrate high quality epitaxial PLD-LSMO flakes on arbitrary substrates with a metal-insulator transition as high as 290 K.

2. Results and Discussion

2.1. Structural Analysis

Figure 1a–d shows the scheme of the fabrication process of epitaxial LSMO membranes. First, the $Sr_{3-x}Ca_xAl_2O_6$ (SC_xAO, $x \leqslant 3$) sacrificial layer is deposited and grown on a (001) $SrTiO_3$ (STO) substrate by solution processing (CSD), Figure 1a. Then, the film is brought into a PLD chamber where an in-vacuum high-temperature re-crystallization process is performed, Figure 1b, followed by the PLD-LSMO deposition, Figure 1c. Finally, the sacrificial layer is water-etched to obtain millimeter sized LSMO membranes supported on a polyethylene terephthalate (PET) sheet, Figure 1d. These membranes can be subsequently transferred to other substrates such as glass and silicon (See Experimental Section for further details).

The surface crystallinity of the films at each stage of the growth process has been monitored by RHEED. Figure 1e–g shows the evolution of the surface crystallinity for the system with SAO sacrificial layer. The as-grown SAO film at 800°C and exposed to air shows no spots indicating an amorphous surface. The film after vacuum thermal annealing at 825°C results in a spotty pattern revealing that the surface recrystallizes, as previously reported.[31] Then, the LSMO film is deposited by PLD on the reconstructed SAO obtaining a new spotty pattern that discloses the formation of an oriented LSMO film, Figure 1g. The same process has been followed to study the behavior of the SC_xAO series with $x \leqslant 3$ and the subsequent growth of the LSMO. From the acquired RHEED patterns (**Figure 2**) it is observed that crystalline films are obtained for all sacrificial layer composition after the vacuum annealing and the crystallinity is transferred to the LSMO films. The periodicity and intensity of the spots identified in the sacrificial layer pattern moderately change as Ca is incorporated in SC_xAO, anticipating changes in the crystallinity and lattice parameter. Slight differences are also appreciated in the shape of the diffraction spots of the LSMO films, which could be attributed to a change in the surface morphology. [55] From the AFM topographic images it is observed that, prior to the LSMO depositions, all SC_xAO films are dense, smooth and homogeneous with a root-mean-square (rms) roughness of ≈1 nm (Figure S1a-d, Supporting Information). After the LSMO deposition, Figure S1e–h (Supporting Information), the films are homogeneous with smooth surfaces of rms ≈2 nm and the size of the grains moderately increases for the LSMO grown on CAO, which is in agreement with the shape of the RHEED pattern.

A separate study was performed to investigate the influence of Ca substitution on the SC_xAO ambient stability. As a case example it is discussed the evolution for SC_2AO composition (see Figure S2, Supporting Information). The as-prepared SC_2AO

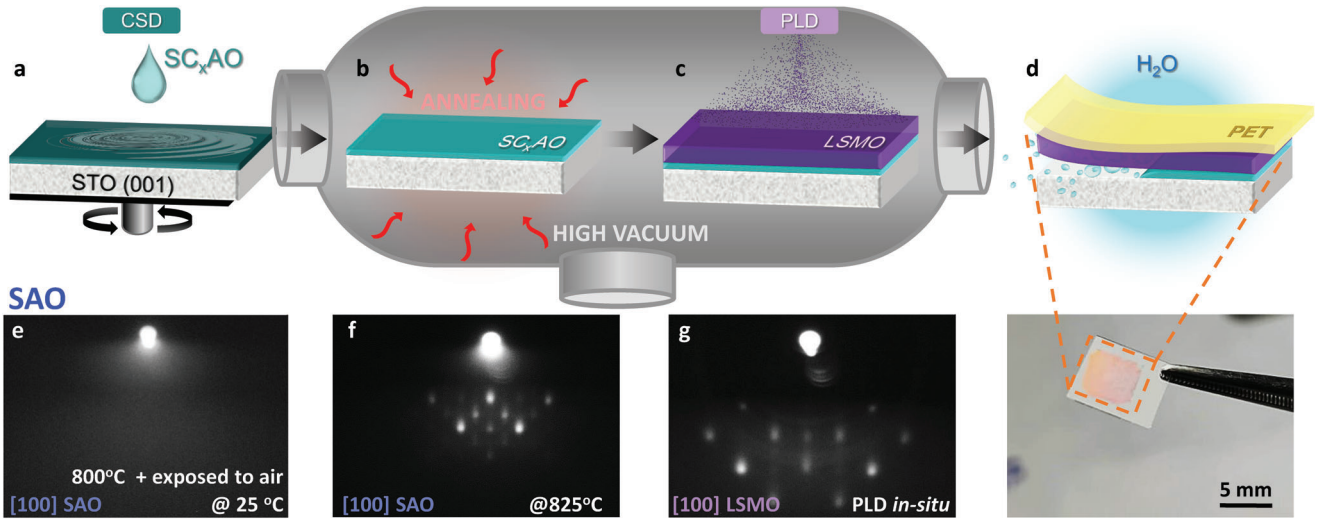

Figure 1. a–d) Sketch of the process followed to fabricate LSMO membranes: a) SC_xAO is grown by CSD on a (001) STO substrate at 800 °C and exposed to air. Then, it is brought to the PLD chamber where b) an annealing treatment up to 825 °C is performed to achieve re-crystallization of the SC_xAO surface and c) LSMO is grown by PLD. d) Finally, the LSMO film can be attached on a polymer support and separated from its original substrate by etching the SC_xAO sacrificial layer in water. Image of a 5 × 5 mm^2 LSMO membrane on a PET support after etching the sacrificial layer. e–g) In situ RHEED analysis of e) SAO after air exposure, f) SAO after vacuum annealing and g) LSMO deposited by PLD.

films after being annealed in vacuum were exposed to air and sealed in plastic bags. RHEED analyses were performed after 7, 16, and 30 days and the samples were stored in sealed plastic bags between experiments. Using this procedure, the surface quality of the samples containing Ca was preserved up to 16 days, Figure S2a (Supporting Information). Longer storage time (i.e. 30 days) results in sample degradation as the spots in the RHEED pattern are significantly less intense and the surface morphology roughens dramatically. Note that by investigating the RHEED pattern of the whole series of vacuum-annealed SC_xAO films after seven days it is found a clear trend in surface crystallinity. The higher the Ca concentration, the more intense the RHEED spots and therefore, more stable (Figure S2b, Supporting Information), in agreement with the expected diminished water sensitivity according to the Ca doping.[30,37] Thus, this study opens the possibility to work in a less-strict environment for the sacrificial layers.

Further structural analysis to study the influence of the sacrificial layer composition on the film crystallinity and subsequent growth of LSMO, was carried out by X-ray diffraction analysis (XRD). **Figure 3**a shows the XRD θ-2θ analysis for the four SC_xAO systems comparing the bare STO contribution, the SC_xAO//STO and the LSMO/SC_xAO//STO. The most intense peak at 2θ= 46.5° corresponds to the (002) STO Bragg reflection and the shoulders appearing next to the STO after growing the different layers can be identified as (008) SC_xAO and (002) LSMO, indicated with $\bigtriangledown$ and *, respectively, in Figure 3a. Focusing on the SC_xAO//STO system, it is observed that by increasing the Ca concentration, the 2θ values of the (008) SC_xAO reflection shifts to higher angles. The shifts in 2θ agree with a change in the c_{SC_xAO} lattice parameter from $c_{SAO}/4 = 3.96$ Å (x = 0) to $c_{CAO}/4 = 3.81$ Å (x = 3). Texture analysis of the SC_xAO films is presented in Table S1, Supporting Information.

After the deposition of the LSMO layer on the in situ vacuum annealed SC_xAO//STO (LSMO/SC_xAO//STO), the (002) LSMO Bragg reflection is observed for all the samples indicating that c-axis oriented growth has been achieved regardless of the Ca composition in the sacrificial, in well agreement with the spotty-streaky RHEED patterns shown in Figure 2e–g. It is

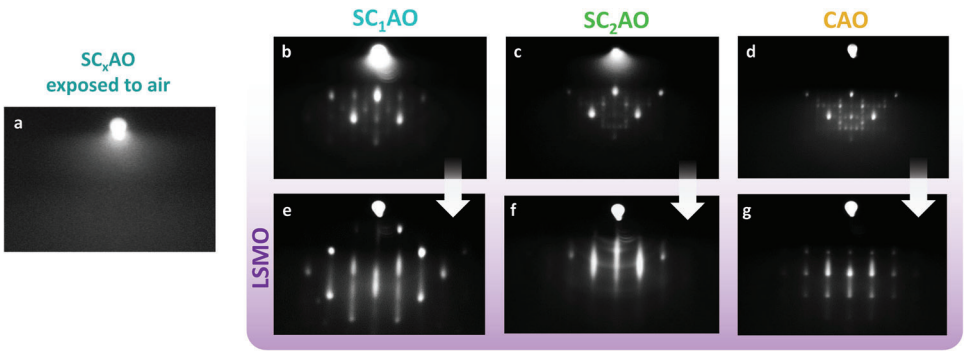

Figure 2. RHEED analysis along the [100] STO of the different SC_xO sacrificial layers a) after air exposure, b–d) after vacuum annealing and e–g) LSMO deposited by PLD.

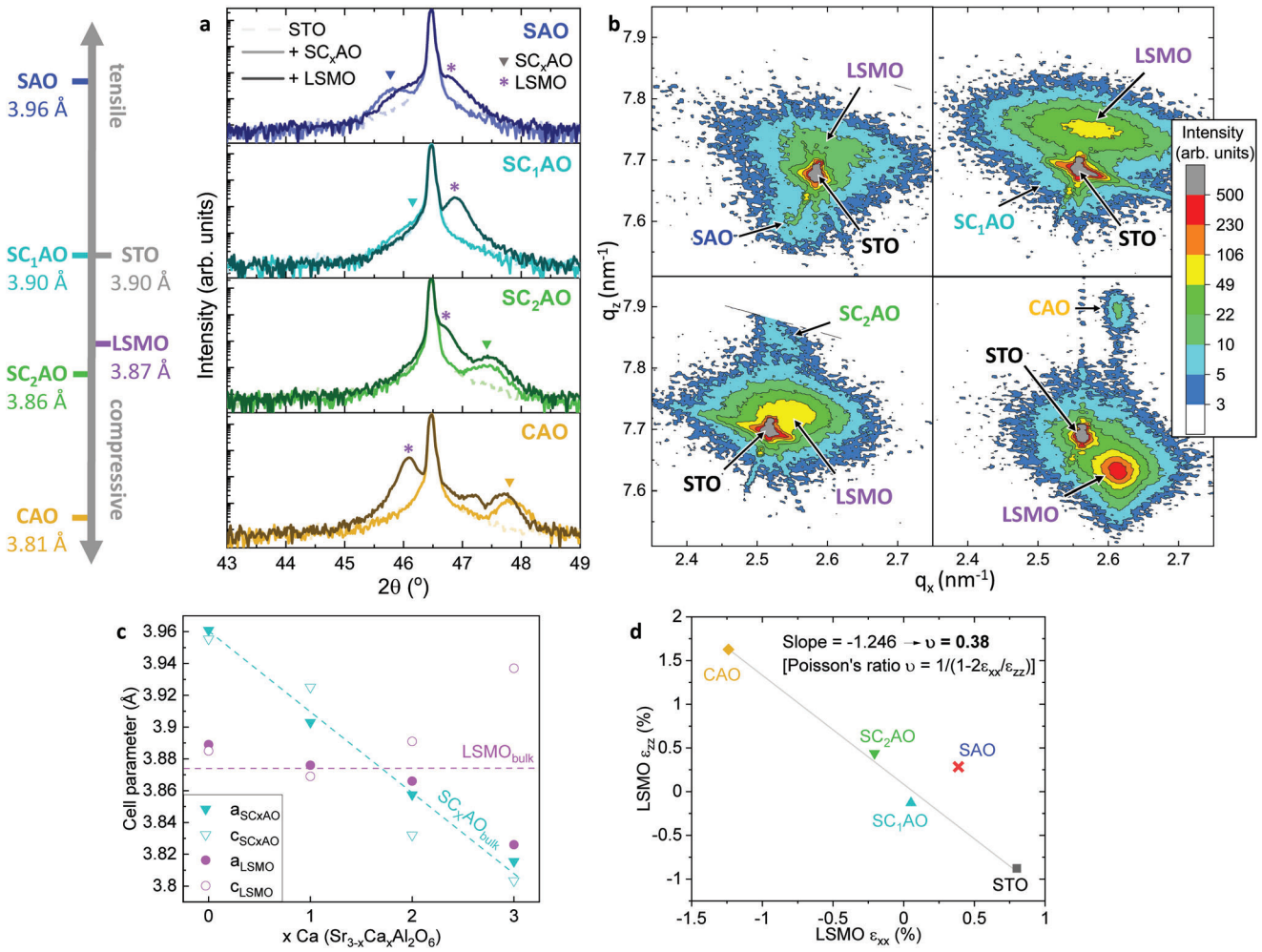

Figure 3. a) XRD θ-2θ scans for the LSMO/SC_xAO//STO heterostructures at each step of the process. ▽ indicates the (008) SC_xAO diffraction peak and * indicates the main (002) LSMO diffraction peak in each case. b) Reciprocal space map around (103) STO reflection for the different LSMO/SC_xAO//STO heterostructures. (103) LSMO and (4 0 12) SC_xAO reflections, indicated in each case, have been used to extract c) the lattice parameters of the SC_xAO and LSMO films. d) Strain in-plane ϵ_{xx} versus strain out-of-plane ϵ_{zz} plot for Poisson's ratio calculation of LSMO films.

noted that the intensity of the (002) LSMO Bragg reflection in the SAO system is slightly lower than the rest. Also, the (008) SAO Bragg reflection for the same system shows a moderate shift toward higher 2θ values. This could indicate that reactivity at the LSMO/SAO occurred, which is in agreement with previous studies on all-vacuum deposited LSMO/SAO system.[34] Also, the heterostructure LSMO/CAO//STO shows an additional peak that appears at $2\theta = 47.2°$ which might be attributed to the formation of a thin layer of a mixed perovskite La-Sr-Mn-Ca-Al-O at the interface.[56] Texture analysis of the LSMO films reveals an improvement of crystalline quality when deposited on Ca-doped SAO, (Table S1 and Figure S3a, Supporting Information) and no further secondary phases are observed in extended XRD θ-2θ scans (Figure S3b, Supporting Information). Remarkably, the 2θ position of the (002) LSMO reflection shifts as a function of the SC_xAO composition suggesting a variation in the LSMO lattice parameter. In order to shed light on these 2θ shifts and the ones observed for the (008) SC_xAO Bragg reflections, high-resolution XRD reciprocal space maps (RSM) have been carried out, see Figure 3b. The most intense peak corresponds to the (103) STO Bragg reflection, whereas less intense and defined peaks appear for (103) LSMO and (4 0 12) SC_xAO. It is noted that the higher the Ca concentration in the sacrificial layer, the more resolved the (4 0 12) SC_xAO and (103) LSMO reflections, strengthening the results of the texture analysis that already indicated an increase in crystalline quality. From the RSM it has been extracted the in-plane (a_{LSMO} and a_{SC_xAO}) and out-of-plane (c_{LSMO} and c_{SC_xAO}) lattice parameters and compared to the respective bulk values, shown in Figure 3c. For the SC_xAO films (cyan symbols) both *a* and *c* lattice parameters decrease by increasing the Ca concentration consistent with the change observed from Figure 3a and in well agreement with Vegard's Law. [57] On the other hand, the lattice parameters of LSMO films (purple symbols) follow a different trend. The lattice parameters of LSMO on SAO and SC_1AO are close to those of the LSMO bulk whereas those of LSMO on SC_2AO and CAO, diverge. Figure 3d depicts the experimental in-plane and out-of-plane strain measured from the LSMO films on the different SC_xAO. The perpendicular strains (ϵ_{xx}, ϵ_{zz}) from

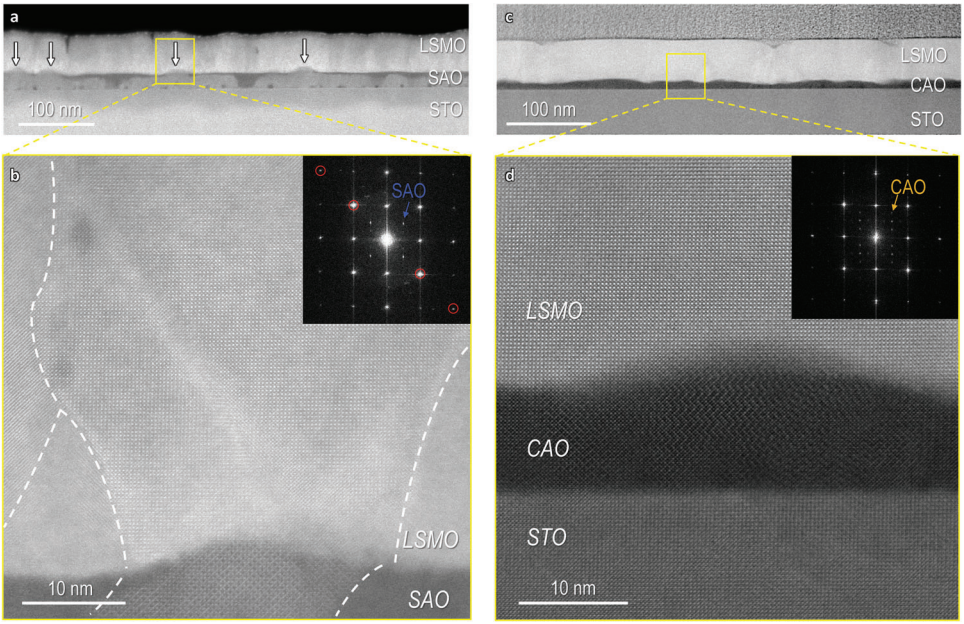

Figure 4. Z-contrast HAADF-STEM cross-sections. a) LSMO/SAO//STO low magnification image. White arrows are used to indicate the formation of outcrops. b) Higher magnification image of one of the outcrops with its corresponding FFT as inset. The LSMO grain boundaries with misoriented grains are marked and their corresponding FFT spots highlighted. c) LSMO/CAO//STO low magnification image. d) Higher magnification image with its corresponding FFT as inset.

LSMO grown on SC_xAO with x=1-3 and from LSMO on STO, follow a linear dependence according to the Poisson effect. This linear trend permits to extract the corresponding Poisson's ratio, ν=0.38, consistent with the values reported for other strained LSMO films.[44] Note that the LSMO grown on SAO does not follow the same strain tendency (Figure 3c). In order to gain insights into this discrepancy and elucidate the possible cation interdiffusion identified from the XRD θ-2θ analysis, cross-sectional Z-contrast high angle annular dark field (HAADF) using scanning transmission electron microscopy (STEM) was carried out for the systems grown on the two extreme compositions: SAO and CAO, **Figure 4**.

First, it is investigated the LSMO/SAO//STO heterostructure, Figure 4a. The low magnification HAADF-STEM image allows identifying the LSMO and SAO layers on STO. The 60 nm LSMO film shows columnar grains, typical of the PLD growth.[58] The SAO film has a thickness of 20 nm with a rough interface with LSMO. It can be identified areas with dark contrast, which corresponds to amorphous SAO and areas with outcrops (white arrows). Regarding the existence of amorphous SAO regions, it reveals that the post-annealing in vacuum performed on SAO films[31] prior to LSMO deposition does not completely reconstruct the surface crystallinity although the spotty RHEED pattern shown in Figure 1f. A closer look at one of these outcrops, Figure 4b, shows the atomic ordering of SAO and LSMO, confirming that it corresponds to epitaxial (001) SAO and it acts as a nucleation site for epitaxial (001) LSMO. From the same magnification image it is also detected the formation of an antiphase boundary (APB) in the center of the (001) LSMO and few (101) oriented LSMO grains whose grain boundaries are identified by dashed white lines. This is further confirmed by fast fourier transform (FFT), red-marked in the inset image in Figure 4b. The nucleation of (101) LSMO grains could be favored by the rough and not completely (001) epitaxial SAO surface. Electron energy loss spectroscopy (EELS) analysis carried out in this region, Figure S4 (Supporting Information), indicates that there is also slight cation interdiffusion between LSMO and SAO, as anticipated from XRD. It is very likely that these two factors, misoriented LSMO grains, and cation diffusion at the interface, favor the growth of an strain-free LSMO film with lower degree of crystallinity,[59] explaining the deviation identified in Figure 3d.

The LSMO/CAO//STO system displays a different landscape. The low magnification image, Figure 4c, confirms the presence of 60 nm LSMO and 10 nm CAO layers on STO. The nature of the Z-contrast HAADF imaging evidence the successful full chemical substitution of Sr by Ca, as the image contrast in the CAO layer is remarkably lower with respect to the SAO layer. Note that the CAO layer is thinner than SAO (20 nm) and it is attributed to different wettability of the precursor solution with the STO substrate. Higher magnification HAADF-STEM image at the LSMO/CAO interface, Figure 4d, confirms the growth of only (001) oriented films, and it is supported by the FFT (inset). The LSMO layer has significantly less amount of structural defects compared to LSMO/SAO (Figure 4b) probably because of the better crystalline quality of the CAO underneath. Therefore, full substitution of Sr by Ca in SC_xAO has an undeniable effect on improving the crystalline quality of the sacrificial and enables the epitaxial growth of moderately strained LSMO films. Nevertheless, it is worth noting that in some areas of the film the LSMO/CAO interface is not sharp and that would be in line with the previous identification of an interfacial reaction. Remarkably, the film microstructure and the interface of the $LSMO/SC_1AO$ system is very similar to the ones presented for the LSMO/CAO, Figure S5 (Supporting Information). Therefore, the

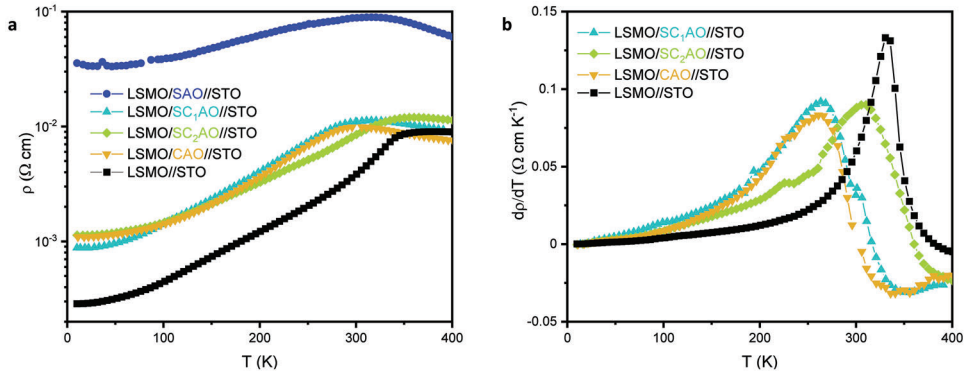

Figure 5. a) Temperature-dependent resistivity of different LSMO/SC_xAO//STO and LSMO//STO heterostructures and b) temperature derivative of the resistivity dρ/dT.

incorporation of Ca with x = 1 in SC_xAO is already causing a significant improvement in epitaxial quality and no amorphous interface has been devised. Overall, from a structural standpoint, the incorporation of Ca in SAO allows tuning the cell parameter while improving the crystalline quality and ambient stability. The epitaxy is transferred to the LSMO generating films with different strains according to the lattice mismatch and surface quality of the SC_xAO underneath. Cation intermixing is spotted in some areas at the LSMO/SC_xAO interface. It is noteworthy that epitaxial LSMO films can be obtained on SC_xAO sacrificial layers after 16 days of being vacuum annealed and stored in sealed plastic bags (Figure S2c, Supporting Information) emphasizing the possibility to combine ex situ and in situ deposition techniques.

2.2. Electrical Properties

To evaluate the electrical properties of LSMO, temperature-dependent resistivity measurements have been carried out on LSMO/SC_xAO//STO heterostructures from 400 to 10K and compared to LSMO//STO. As shown in **Figure 5**a, all LSMO films show a metallic behavior, however, the resistivity of the LSMO on SAO is significantly higher than the rest. This performance is not surprising considering the LSMO/SAO microstructure unraveled from Figure 4 and in agreement with previous reports on the impact of microstructure on the electrical transport properties.[46,60] Focusing on LSMO on Ca-doped SAO heterostructures and LSMO//STO, they all show similar resistivity values at room temperature. Nonetheless, the temperature dependence of the resistivity shows variations that are more pronounced for LSMO//STO. Note that the ρ(T) data presented here for LSMO/SC_xAO (x = 1-3) follow the same trend and fall within the same order of magnitude of the reported values from the literature. [24,54] Also, changes in the metal to insulator transition, T_{MI}, can be appreciated from the resistance derivative curve in Figure 5b. These changes could be attributed to the presence of different degrees of epitaxial strain, calculated in Figure 3d, although no clear trend is observed for the heterostructures. The interfacial reactivity is also expected to produce changes in the electrical properties. Indeed, it has been widely reported the important role of ion stoichiometry in LSMO (oxygen deficiency, cation off-stoichiometry, Sr-segregation, interdiffusion) on the temperature-dependent resistivity.[61–63] Thus, further STEM-EELS analysis would be useful to probe the interface of our LSMO heterostructures with atomic precision to elucidate its possible role.

2.3. Freestanding Epitaxial LSMO

The last step to obtain freestanding epitaxial LSMO films requires adhering a support layer, in our case PET, to easily manipulate the membrane upon the sacrificial etching in water, **Figure 6**a. Also, the PET can be used as a stamp to further transfer the LSMO released membranes to other substrates with no epitaxial relationship, e.g., glass or Si wafer. Importantly, we verified that the concentration of Ca in SC_xAO affects the immersion time in water of the heterostructure being SAO the fastest (2 days) and CAO the slowest (2 weeks), as expected.[37]

The LSMO//PET stacks obtained from the different SC_xAO compositions show smooth and homogeneous surface morphology (Figure S1i–l, Supporting Information) and only show the (002) LSMO Bragg reflection, Figure 6b, which is centered at the 2θ value of LSMO-bulk. Therefore, all membranes on PET are fully relaxed. Optical inspection of the different LSMO membranes disclosed the formation of cracks. The density of cracks increases with the content of Ca in SC_xAO, Figure 6e–g and it can be quantified (details in Figure S6, Supporting Information) and compared to the strain release for each LSMO/SC_xAO system.[64] From Figure 6c it can be observed that the least strained LSMO on SC_xAO, i.e., on SC_1AO, generated least cracks. By increasing the amount of Ca in the sacrificial, the LSMO films show moderate compressive strain and upon release they also show more cracks. It is suggested that the strain relaxation during the lift-off can be responsible for the formation of cracks,[65] as previously reported in $BaSnO_3$ membranes.[37] Nevertheless, there are other factors that could be investigated to further reduce the crack density of the released membranes, including the sacrificial layer and membrane thicknesses,[20] the use of additional capping layers[36,64] and modify the lift-off procedure.[35,66] Indeed, the exfoliation process is one of the most critical steps in the preparation of membranes.[67]

Additional membrane analysis was performed on the LSMO obtained from SC_2AO which showed the best compromise

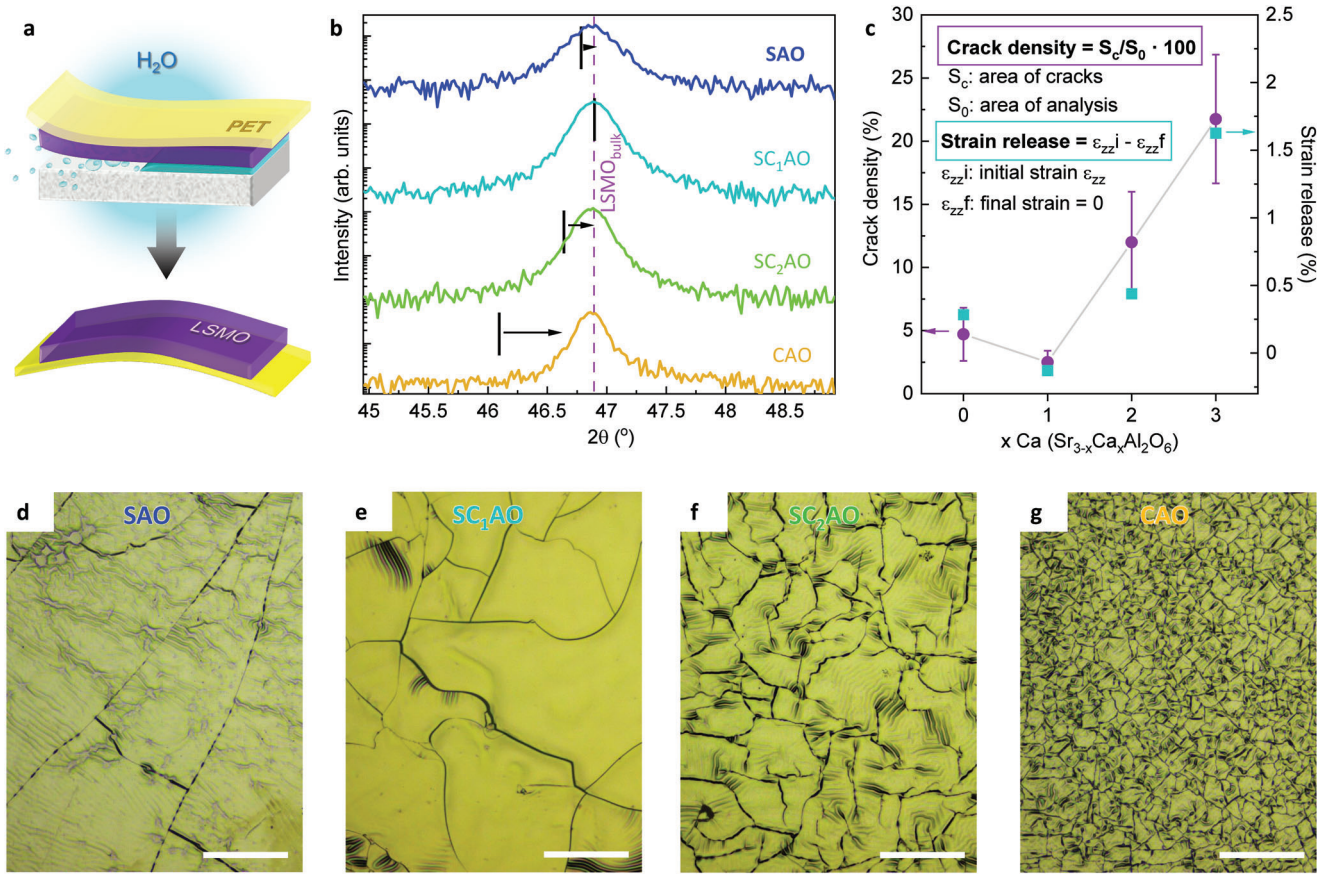

Figure 6. Freestanding LSMO on PET after the selective etching of the SC_xAO sacrificial layers. a) Sketch of the process followed to transfer LSMO membranes to a PET support. b) XRD θ-2θ scans of the LSMO membranes supported on PET. The black bar indicates the position of the (002) LSMO Bragg reflection before the lift-off. c) Crack density and strain release of LSMO membranes as a function of the Ca concentration of the SC_xAO sacrificial layer. Magnified images of the corresponding LSMO membranes on PET by etching d) SAO, e) SC_1AO, f) SC_2AO, and g) CAO. White scale bars correspond to 200 µm.

between crystallinity, electrical performance (T_{MI}=310 K), moderate crack density, and can be released faster than from CAO. X-ray photoelectron spectroscopy (XPS) survey spectrum revealed the presence of Al traces on the LSMO membrane, which was further verified from Al2p core level spectrum (Figure S7, Supporting Information). This chemical analysis reafirmed the cation intermixing at the interface LSMO/SC_xAO.

Then, this LSMO membrane was double-transferred onto a rigid Si substrate, **Figure 7**a, to perform HAADF-STEM studies. Figure 7b proves the high crystallinity of the LSMO membrane integrated into silicon, a highly pursued goal to widen the possibilities of silicon-based electronics.[68–71] The temperature-dependent resistivity of the LSMO membrane prepared from SC_2AO was also evaluated by transferring it to a glass substrate. Electrical measurements were performed by patterning gold contacts on top of a flake with no cracks. The resistivity curves obtained before and after the transferring are very similar (Figure 7c) , indicating that there is almost no degradation of the film during the transferring process. The small differences in the LSMO resistivity before and after the release could be attributed to the strain relaxation of the film.[24]

Finally, it is important to note that the hybrid process here presented to prepare epitaxial membranes which combines solution processed SC_xAO sacrificial layers with PLD deposition of LSMO, could be easy extended to other perovskite systems and beyond, such as spinels. In Figure S8 (Supporting Information) it is shown a RHEED study analogous to that presented in Figure 2 for the preparation of PLD-$CoFe_2O_4$ on solution processed SC_xAO confirming the growth of crystalline and oriented $CoFe_2O_4$ films.

3. Conclusion

In this study, we put forward a simple hybrid synthesis procedure combining solution processing and pulsed laser deposition to easily prepare epitaxial complex oxide membranes. First, it is investigated the influence of gradual Ca-substitution in solution processed SAO films (SC_xAO with $x \leqslant 3$) to effectively engineer its crystallinity, structure, and robustness preserving a smooth surface. Moreover, it has been demonstrated that vacuum annealing of SC_xAO after air exposure reconstructs the surface crystallinity and increases their stability in air offering a less-strict environment to prepare and manipulate the sacrificial layers. The composition of SC_xAO influences the properties of the subsequent epitaxial LSMO film. Ca substitution in SC_xAO favors better crystallinity inducing slight compressive

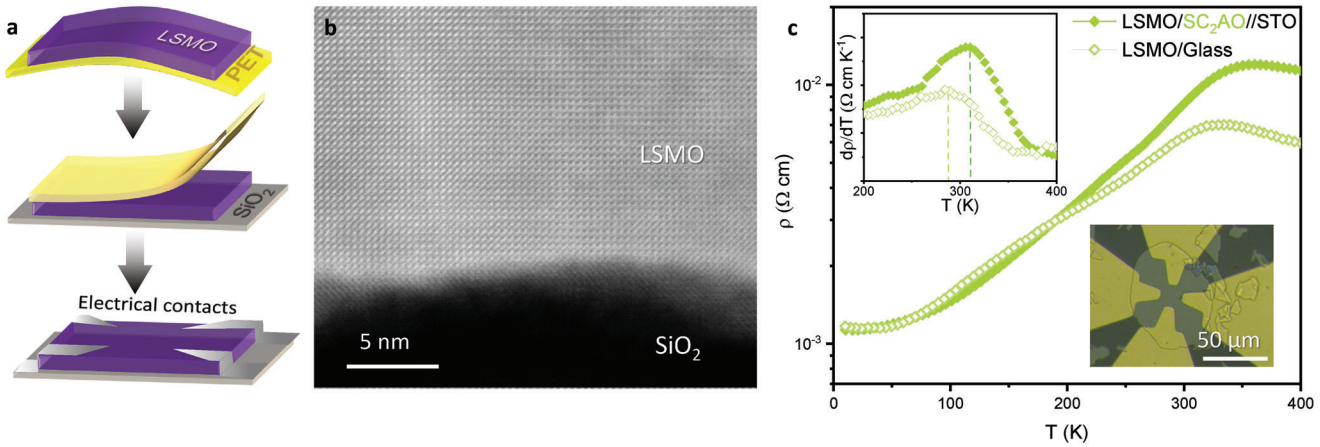

Figure 7. a) LSMO membranes transferred from a PET support to other substrates such as SiO_2 (300 nm)/Si or glass, which were used to make the electrical contact of the transferred LSMO. b) Z-contrast HAADF-STEM cross-section of LSMO//SiO_2 interface. c) Temperature-dependent resistivity of the released LSMO membrane. Upper inset shows the temperature derivative of the resistivity dρ/dT. Lower inset corresponds to a magnified image of a LSMO flake with the contacts for the resistivity measurements.

strain that is totally released upon LSMO exfoliation generating cracks. Improving the functional complex oxide/sacrificial interface quality and improving the lift-off process is still required, but epitaxial LSMO membranes can be obtained while maintaining the metallic behavior identified prior the lift-off. Therefore, this study provides an innovative and versatile platform to synthesize complex oxide freestanding films and heterostructures that can be integrated in a wide variety of substrates in the search for novel and enhanced properties envisaging many technological benefits.

4. Experimental Section

Synthesis of SC_xAO Sacrificial Layer by CSD: SC_xAO sacrificial layers with different ratios of Ca (x = 0, 1, 2, 3) were epitaxially grown on (001) STO single-crystal substrates by chemical solution deposition. For each composition, a solution was prepared with stoichiometric amounts of $Sr(NO_3)_2$, strontium nitrate (>99%), $Ca(NO_3)_2$, calcium nitrate (>99%), and $Al(NO_3)_3{\cdot}9H_2O$, hydrated aluminum nitrate (>98%), which were dissolved in Milli-Q water with citric acid, $C_6H_8O_7$ (>99%), to obtain a 0.1 M solution. This solution was spin-coated on STO and annealed in a tubular furnace at 800 °C under 0.6 l·min^{-1} O_2 flow to finally obtain a 20 nm thick film. This route was previously developed and optimized for SAO sacrificial layer and it is described with further details elsewhere.[26]

Ex Situ Synthesis of Epitaxial LSMO by PLD: Following the growth of SC_xAO, upon sample air-exposure, the film was introduced in the PLD chamber to perform an in-vacuum annealing up to 825 °C for 30 min at an oxygen partial pressure PO_2 of 0.1 mbar to restore the SC_xAO surface crystallinity.[31] Then, 60 nm thick LSMO films were epitaxially grown in situ by PLD at 725 °C and a PO_2 of 0.1 mbar using a KrF excimer laser. The same PLD growing conditions were used to prepare LSMO directly on a (001) STO substrate. On the other hand, a similar PLD process was followed to grow $CoFe_2O_4$ on SAO//STO, Figure S8 (Supporting Information).

Membrane Transfer: The transfer of the LSMO thin films deposited on SC_xAO//STO was done adhering a polyethylene terephthalate (PET) polymer support to the film before immersing the entire heterostructure in Milli-Q water. Once the SC_xAO sacrificial layer was completely etched, the PET was mechanically separated achieving the membrane of LSMO attached on it. For specific analysis, the membrane held on PET was subsequently transferred to silicon or glass.

Crystal Structure: X-ray Diffraction (XRD) measurements were performed with Cu-Kα using a Bruker-AXS (model A25 D8 Discover). Reflection high-energy electron diffraction (RHEED) was performed in the PLD chamber during SC_xAO re-crystallization and LSMO deposition with incidence of electrons along the [100] STO at a glancing angle of 1–2°. Aberration-corrected Scanning Transmission Electron Microscopy (STEM) imaging was performed using a Nion HERMES-100, operated at 60 kV, at the University of Chinese Academy of Sciences, Beijing, China. High-angle annular dark-field (HAADF) images were acquired using an annular detector with collection semi-angle of 75–210 mrad. To minimize the possible beam-induced structural damage on the SAO films, images were acquired with reduced beam current (10 pA). Electron energy loss spectroscopy (EELS) measurements were performed using a collection semi-angle of 75 mrad, an energy dispersion of 0.9 eV per channel, and a probe current of ≈10 pA. Cross-sectional STEM specimens were prepared using the standard focused ion beam (FIB) lift-out process in a Thermo Fisher Scientific FIB system. Protective amorphous carbon and thin Pt layers were applied over the region of interest before milling. To minimize the sidewall damage and sufficiently thin the specimen for electron transparency, final milling was carried out at a voltage of 2 kV.

Surface Morphology: Atomic Force Microscopy (AFM) was used to study the surface morphology and roughness of the samples. Topographic images of 5 × 5 μm^2 were acquired with a Keysight 5100 AFM instrument and analyzed by Mountains8 software. An optical microscope Leica DM1750 M was used to take magnified optical images of the transferred membranes and analyze the crack density.

Electrical Properties: Resistivity curves, ρ(T) were measured using the Van der Pauw configuration[72] in a Physical Properties Measurement System (PPMS) from Quantum Design. 50 nm thick gold contacts were prepared by standard photolithography combined by lift-off. In the case of the transferred LSMO, patterned contacts were placed on top of a single flake (see Figure 7c).

Supporting Information

Supporting Information is available from the Wiley Online Library or from the author.

Acknowledgements

This work was funded by MICIN/AEI/10.13039/ 501100011033/FEDER through the projects Severo Ochoa FUNFUTURE CEX2019-00917-S,

CEX2021-001214-S and PID2020-114224RBI00, TED2021-130402B-I00. The authors also acknowledge the financial support from the 2020 Leonardo Grant for Researchers and Cultural Creators BBVA Foundation, the i-link A20346-CSIC project, the National Key RD Program of China (2018YFA0305800), and the Beijing Outstanding Young Scientist Program (BJJWZYJH01201914430039). The project that gave rise to these results received the support of a fellowship (P.S.) from "la Caixa" Foundation (ID 100010434). The fellowship code was LCF/BQ/DI19/11730026. M.R. acknowledges the support from FPI fellowship PRE2021-099672. The authors are thankful to the Thin film scientific service at ICMAB and to Dr. J. Santiso from ICN2 for the fruitful discussions on structure properties. This work had been done in the framework of the doctorate in material science of the Autonomous University of Barcelona (P.S. and M.R.).

Conflict of Interest

The authors declare no conflict of interest.

Data Availability Statement

Research data are not shared.

Keywords

freestanding oxides, interfaces, $La_{0.7}Sr_{0.3}MnO_3$, sacrificial layers, solution processing, $Sr_3Al_2O_6$

Received: April 12, 2023
Revised: May 18, 2023
Published online: June 15, 2023

[1] M. Coll, J. Fontcuberta, M. Althammer, M. Bibes, H. Boschker, A. Calleja, G. Cheng, M. Cuoco, R. Dittmann, B. Dkhil, I. El Baggari, M. Fanciulli, I. Fina, E. Fortunato, C. Frontera, S. Fujita, V. Garcia, S. Goennenwein, C.-G. Granqvist, J. Grollier, R. Gross, A. Hagfeldt, G. Herranz, K. Hono, E. Houwman, M. Huijben, A. Kalaboukhov, D. Keeble, G. Koster, L. Kourkoutis, et al., *Appl. Surf. Sci.* **2019**, *482*, 1.
[2] Q. Lin, H. Huang, Y. Jing, H. Fu, P. Chang, D. Li, Y. Yao, Z. Fan, *J. Mater. Chem. C* **2014**, *2*, 1233.
[3] Y. S. Rim, S. Bae, H. Chen, N. De Marco, Y. Yang, *Adv. Mater.* **2016**, *28*, 4415.
[4] J. F. Scott, *Science* **2007**, *315*, 954.
[5] P. Machado, M. Scigaj, J. Gazquez, E. Rueda, A. Sánchez-Díaz, I. Fina, M. Gibert-Roca, T. Puig, X. Obradors, M. Campoy-Quiles, M. Coll, *Chem. Mater.* **2019**, *31*, 947.
[6] Z. Liao, F. Li, P. Gao, L. Li, J. Guo, X. Pan, R. Jin, E. W. Plummer, J. Zhang, *Phys. Rev. B* **2015**, *92*, 125123.
[7] X. Obradors, T. Puig, *Supercond. Sci. Technol.* **2014**, *27*, 044003.
[8] R. L. Z. Hoye, J. Hidalgo, R. A. Jagt, J.-P. Correa-Baena, T. Fix, J. L. MacManus-Driscoll, *Adv. Energy Mater.* **2021**, *12*, 59.
[9] S. A. Chambers, *Adv. Mater.* **2010**, *22*, 219.
[10] G. Koster, M. Huijben, G. Rijnders, *Epitaxial Growth of Complex Metal Oxides*, 1st Ed., Elsevier, Amsterdam **2015**.
[11] J. L. MacManus-Driscoll, M. P. Wells, C. Yun, J.-W. Lee, C.-B. Eom, D. G. Schlom, *APL Mater.* **2020**, *8*, 040904.
[12] M. Brahlek, A. S. Gupta, J. Lapano, J. Roth, H.-T. Zhang, L. Zhang, R. Haislmaier, R. Engel-Herbert, *Adv. Funct. Mater.* **2018**, *28*, 1702772.
[13] D. Pesquera, A. Fernández, E. Khestanova, L. W. Martin, *J. Phys.: Condens. Matter* **2022**, *34*, 383001.
[14] S. Han, Y. Meng, Z. Xu, J. S. Kim, Y. Li, I.-P. Roh, H. Ahn, D.-H. Kim, S.-H. Bae, *ACS Appl. Electron. Mater.* **2023**, *5*, 690.
[15] H. Yoon, T. K. Truttmann, F. Liu, B. E. Matthews, S. Choo, Q. Su, V. Saraswat, S. Manzo, M. S. Arnold, M. E. Bowden, J. K. Kawasaki, S. J. Koester, S. R. Spurgeon, S. A. Chambers, B. Jalan, *Sci. Adv.* **2022**, *8*, 51eadd5328.
[16] K. T. Kang, J. Park, D. Suh, W. S. Choi, *Adv. Mater* **2019**, *31*, 1803732.
[17] G. Rijnders, D. H. A. Blank, *Nature* **2005**, *433*, 369.
[18] S. Puebla, T. Pucher, V. Rouco, G. Sanchez-Santolino, Y. Xie, V. Zamora, F. A. Cuellar, F. J. Mompean, C. Leon, J. O. Island, M. Garcia-Hernandez, J. Santamaria, C. Munuera, A. Castellanos-Gomez, *Nano Lett.* **2022**, *22*, 7457.
[19] C. Guo, H. Huang, *Microstructures* **2022**, *2*, 21.
[20] S. S. Hong, M. Gu, M. Verma, V. Harbola, B. Y. Wang, D. Lu, A. Vailionis, Y. Hikita, R. Pentcheva, J. M. Rondinelli, H. Y. Hwang, *Science* **2020**, *368*, 71.
[21] Z. Dong, H. Chen, M. Qi, J. Shen, W. Liu, E. Guo, D. Li, Y. Zhang, Z. Wu, *Laser Photonics Rev.* **2022**, *16*, 2100454.
[22] S. Cai, Y. Lun, D. Ji, P. Lv, L. Han, C. Guo, Y. Zang, S. Gao, Y. Wei, M. Gu, C. Zhang, Z. Gu, X. Wang, C. Addiego, D. Fang, Y. Nie, J. Hong, P. Wang, X. Pan, *Nat. Commun* **2022**, *13*, 5116.
[23] F. M. Chiabrera, S. Yun, Y. Li, R. T. Dahm, H. Zhang, C. K. R. Kirchert, D. V. Christensen, F. Trier, T. S. Jespersen, N. Pryds, *Ann. Phys.* **2022**, *524*, 2200084.
[24] D. Lu, D. J. Baek, S. S. Hong, L. F. Kourkoutis, Y. Hikita, H. Hwang, *Nat. Mater.* **2016**, *15*, 1255.
[25] D. Ji, S. Cai, T. R. Paudel, H. Sun, C. Zhang, L. Han, Y. Wei, Y. Zang, M. Gu, Y. Zhang, W. Gao, H. Huyan, W. Guo, D. Wu, Z. Gu, E. Y. Tsymbal, P. Wang, Y. Nie, X. Pan, *Nature* **2019**, *570*, 87.
[26] P. Salles, I. Caño, R. Guzman, C. Dore, A. Mihi, W. Zhou, M. Coll, *Adv. Mater. Interfaces* **2021**, *8*, 2001643.
[27] J. A. Alonso, I. Rasines, J. L. Soubeyroux, *Inorg. Chem.* **1990**, *29*, 4768.
[28] Y.-Y. Pai, A. Tylan-Tyler, P. Irvin, J. Levy, *Rep. Prog. Phys.* **2018**, *81*, 036503.
[29] A. S. Brand, J. W. Bullard, *Langmuir* **2017**, *33*, 9645.
[30] A. K. Prodjosantoso, B. J. Kennedy, B. A. Hunter, *Aust. J. Chem.* **2000**, *53*, 195.
[31] P. Salles, R. Guzmán, D. Zanders, A. Quintana, I. Fina, F. Sánchez, W. Zhou, A. Devi, M. Coll, *ACS Appl. Mater. Interfaces* **2022**, *14*, 12845.
[32] D. Li, C. Adamo, B. Y. Wang, H. Yoon, Z. Chen, S. S. Hong, D. Lu, Y. Cui, Y. Hikita, H. Y. Hwang, *Nano Lett.* **2021**, *21*, 4454.
[33] Y. Li, C. Xiang, F. M. Chiabrera, S. Yun, H. Zhang, D. J. Kelly, R. T. Dahm, C. K. R. Kirchert, T. E. L. Cozannet, F. Trier, D. V. Christensen, T. J. Booth, S. B. Simonsen, S. Kadkhodazadeh, T. S. Jespersen, N. Pryds, *Adv. Mater.* **2022**, *34*, 2203187.
[34] D. J. Baek, D. Lu, Y. Hikita, H. Y. Hwang, L. F. Kourkoutis, *APL Mater.* **2017**, *5*, 096108.
[35] J. Bouaziz, C. Cancellieri, B. Rheingans, L. P. H. Jeurgens, F. La Mattina, *Adv. Mater. Interfaces* **2022**, *10*, 2201458.
[36] L. Gong, M. Wei, R. Yu, H. Ohta, T. Katayama, *ACS Nano* **2022**, *16*, 21013.
[37] P. Singh, A. Swartz, D. Lu, S. S. Hong, K. Lee, A. F. Marshall, K. Nishio, Y. Hikita, H. Y. Hwang, *ACS Appl. Electron. Mater.* **2019**, *1*, 1269.
[38] R. Xu, J. Huang, E. S. Barnard, S. S. Hong, P. Singh, E. K. Wong, T. Jansen, V. Harbola, J. Xiao, B. Y. Wang, S. Crossley, D. Lu, S. Liu, H. Y. Hwang, *Nat. Commun.* **2020**, *11*, 3141.
[39] Z. Lu, Y. Yang, L. Wen, J. Feng, B. Lao, X. Zheng, S. Li, K. Zhao, B. Cao, Z. Ren, D. Song, H. Du, Y. Guo, Z. Zhong, X. Hao, Z. Wang, R.-W. Li, *npj Flex Electron* **2022**, *6*, 9.
[40] J.-H. Park, E. Vescovo, H.-J. Kim, C. Kwon, R. Ramesh, T. Venkatesan, *Nature* **1998**, *392*, 794.
[41] Y. Wu, Y. Suzuki, U. Rüdiger, J. Yu, A. D. Kent, T. K. Nath, C. B. Eom, *Appl. Phys. Lett.* **1999**, *75*, 2295.
[42] M. Cesaria, A. P. Caricato, G. Maruccio, M. Martino, *J. Phys. Conf. Ser.* **2011**, *292*, 012003.
[43] Y. Takamura, R. V. Chopdekar, E. Arenholz, Y. Suzuki, *Appl. Phys. Lett.* **2008**, *92*, 162504.

[44] C. Adamo, X. Ke, H. Q. Wang, H. L. Xin, T. Heeg, M. E. Hawley, W. Zander, J. Schubert, P. Schiffer, D. A. Muller, L. Maritato, D. G. Schlom, *Appl. Phys. Lett.* **2009**, *95*, 112504.
[45] B. Wang, L. You, P. Ren, X. Yin, Y. Peng, B. Xia, L. Wang, X. Yu, S. Mui Poh, P. Yang, G. Yuan, L. Chen, A. Rusydi, J. Wang, *Nat. Commun.* **2013**, *4*, 2778.
[46] J. Fontcuberta, M. Bibes, B. Martínez, V. Trtik, C. Ferrater, F. Sánchez, M. Varela, *J. Appl. Phys.* **1999**, *85*, 4800.
[47] M. Sirena, N. Haberkorn, M. Granada, L. B. Steren, J. Guimpel, *J. Appl. Phys.* **2009**, *105*, 033902.
[48] C. Ge, K.-J. Jin, L. Gu, L.-C. Peng, Y.-S. Hu, H.-Z. Guo, H.-F. Shi, J.-K. Li, J.-O. Wang, X.-X. Guo, C. Wang, M. He, H.-B. Lu, G.-Z. Yang, *Adv. Mater. Interfaces* **2015**, *2*, 1500407.
[49] Z. Fang, I. V. Solovyev, K. Terakura, *Phys. Rev. Lett.* **2000**, *84*, 3169.
[50] J. Huang, H. Wang, X. Sun, X. Zhang, H. Wang, *ACS Appl. Mater. Interfaces* **2018**, *10*, 42698.
[51] W. Hou, S. Zhao, T. Wang, M. Yao, W. Su, Z. Hu, Z. Zhou, M. Liu, *Appl. Surf. Sci.* **2021**, *563*, 150074.
[52] C.-C. Chiu, Y.-W. Chang, Y.-C. Shao, Y.-C. Liu, J.-M. Lee, S.-W. Huang, W. Yang, J. Guo, F. M. F. de Groot, J.-C. Yang, Y.-D. Chuang, *Sci. Rep.* **2021**, *11*, 5250.
[53] D. J. Baek, D. Lu, Y. Hikita, H. Y. Hwang, L. F. Kourkoutis, *ACS Appl. Mater. Interfaces* **2017**, *9*, 54.
[54] Z. Lu, J. Liu, J. Feng, X. Zheng, L.-h. Yang, C. Ge, K.-j. Jin, Z. Wang, R.-W. Li, *APL Mater.* **2020**, *8*, 051105.
[55] D. O'Connor, B. Sexton, R. Smart, *Surface Analysis Methods in Materials Science*, 2 Ed., Springer, Berlin **2003**.
[56] A. M. Deml, V. Stevanović, A. M. Holder, M. Sanders, R. O'Hayre, C. B. Musgrave, *Chem. Mater.* **2014**, *26*, 6595.
[57] A. R. Denton, N. W. Ashcroft, *Phys. Rev. A* **1991**, *43*, 3161.
[58] O. I. Lebedev, G. V. Tendeloo, S. Amelinckx, H. L. Ju, K. M. Krishnan, *Philos. Mag. A* **2000**, *80*, 673.
[59] Y. Chen, J. A. Tilka, Y. Ahn, J. Park, A. Pateras, T. Zhou, D. E. Savage, I. McNulty, M. V. Holt, D. M. Paskiewicz, D. D. Fong, T. F. Kuech, P. G. Evans, *J. Phys. Chem. C* **2019**, *123*, 7447.
[60] J. Santiso, J. Roqueta, N. Bagués, C. Frontera, Z. Konstantinovic, Q. Lu, B. Yildiz, B. Martínez, A. Pomar, L. Balcells, F. Sandiumenge, *ACS Appl. Mater. Interfaces* **2016**, *8*, 16823.
[61] J. D. Burton, E. Y. Tsymbal, *Phys. Rev. Lett.* **2011**, *106*, 157203.
[62] H. Zenia, G. A. Gehring, G. Banach, W. M. Temmerman, *Phys. Rev. B* **2005**, *71*, 024416.
[63] Z. Liao, J. Zhang, *Appl. Sci.* **2019**, *9*, 144.
[64] Q. Wang, H. Fang, D. Wang, J. Wang, N. Zhang, B. He, W. Lü, *Crystals* **2020**, *10*, 733.
[65] H. Taghinejad, A. A. Eftekhar, P. M. Campbell, B. Beatty, M. Taghinejad, Y. Zhou, C. J. Perini, H. Moradinejad, W. E. Henderson, E. V. Woods, X. Zhang, P. Ajayan, E. J. Reed, E. M. Vogel, A. Adibi, *NPJ 2D Mater. Appl.* **2018**, *2*, 1.
[66] B. Zhang, C. Yun, J. L. MacManus-Driscoll, *Nano-Micro Lett.* **2021**, *13*, 39.
[67] A. Castellanos-Gomez, V. Singh, H. S. J. van der Zant, G. A. Steele, *Ann. Phys.* **2015**, *527*, 1-227.
[68] U. K. Bhaskar, N. Banerjee, A. Abdollahi, Z. Wang, D. G. Schlom, G. Rijnders, G. Catalan, *Nat. Nanotechnol.* **2016**, *11*, 263.
[69] A. Gómez, J. M. Vila-Fungueiriño, R. Moalla, G. Saint-Girons, J. Gázquez, M. Varela, R. Bachelet, M. Gich, F. Rivadulla, A. Carretero-Genevrier, *Small* **2017**, *13*, 1701614.
[70] J. M. Vila-Fungueiriño, J. Gázquez, C. Magén, G. Saint-Girons, R. Bachelet, A. Carretero-Genevrier, *Sci. Technol. Adv. Mater.* **2018**, *19*, 702.
[71] D. P. Kumah, J. H. Ngai, L. Kornblum, *Adv. Funct. Mater.* **2020**, *30*, 1901597.
[72] L. J. Van der Pauw, *Philips Tech. Rev.* **1958**, *13*, 1.